# The Stability and Evolution of Curved Domains Arising from One-Dimensional Localized Patterns[*]

Karl B. Glasner[†] and Alan E. Lindsay[‡]

**Abstract.** In many pattern forming systems, narrow two-dimensional domains can arise whose cross sections are roughly one-dimensional localized solutions. This paper investigates this phenomenon in the variational Swift–Hohenberg equation. Stability of straight line solutions is analyzed, leading to criteria for either curve buckling or curve disintegration. Matched asymptotic expansions are used to derive a two-term expression for the geometric motion of curved domains, which includes both elastic and surface diffusion-type regularizations of curve motion. This leads to novel equilibrium curves and space-filling pattern proliferation. Numerical tests are used to confirm and illustrate these phenomena.

## 1. Introduction.

Pattern forming systems such as the Swift–Hohenberg equation,

$$(1.1) \qquad u_t = ru - (1 + \Delta)^2 u + N(u), \quad u : \mathbb{R}^2 \to \mathbb{R},$$

often possess a super- or subcritical bifurcation which leads to a finite wavelength instability (for (1.1) this occurs where $r > 0$). This instability and the ensuing nonlinear evolution has been well studied (see, for example, the review [8]) and leads to a wide variety of behaviors, such as the formation of stripes and hexagonal patterns throughout the domain.

In the case where the bifurcation is subcritical, there may be pattern formation even when $r < 0$ and the base state $u \equiv 0$ is stable. This can take the form of localized steady states [3, 6, 9, 16] or self-replication [14, 19, 26, 28], where a patterned state may invade the base state.

In problems such as (1.1), where the dynamics satisfy a variational principle, it is natural to compare energies of the flat base state to some candidate steady pattered state. Parameter values which lead to equal energy are called the *Maxwell points* (which is typically a curve if the parameter space is two-dimensional) [27]. Remarkably, stationary fronts exist not just at the Maxwell point, but in an interval around the Maxwell point called the *pinning region*.

Related to stationary fronts are spatially localized states (used here to mean steady solutions which decay exponentially). It is understood these can be created by placing stationary fronts back-to-back. As with fronts, they only exist within the pinning region. The bifurcation diagram for steady localized states contains branches which oscillate from one side of the pinning region to the other, as well as secondary branches connecting these [4, 17, 30]. Because of their appearance on the bifurcation diagram of solutions, these branches are whimsically referred to as *snakes* and *ladders.*

There are several recent explanations of the ubiquity of snaking bifurcations (see also the reviews [9] and [16]). The approach of Chapman and Kozyreff [6] is an asymptotic analysis, perturbing around the Maxwell point and base state simultaneously. They show in a rather nontrivial fashion that it is exponentially small terms (in a small parameter representing pattern amplitude) that give rise to the bifurcation diagram. Another complementary description of events was offered by Beck et al. [3], whereby localized states were characterized as intersections of stable and unstable manifolds of a two-dimensional map. Bifurcations of steady states arise from the interwoven nature of these manifolds.

Two-dimensional steady patterns may also arise from similar considerations. The simplest situation is a stripe whose cross section is a one-dimensional localized state [4]. There are also steady states which are genuinely two-dimensional. Localized patterns have been identified having radial symmetry [21, 23], hexagonal substructure [22], and striped substructure [2].

Dynamical proliferation of pattern domains in higher dimensions is also commonly observed [15, 24, 25]. Of particular note are bilayer-type interfaces whose propagation is a function of curvature and its derivatives [13]. In the present context, these domains are curves whose cross section profiles are roughly one-dimensional localized states. One would expect, therefore, that depending on where the system lies relative to the Maxwell point, these domains will enlarge or contract. How this occurs is the subject of this paper.

We begin with a discussion of striped domains and analyze their stability (section 2). We find that stripes can, under certain circumstances, persist as narrow curved domains. In this case, the evolution of more general curved stripes is derived (section 3) by a matched asymptotic expansion. The leading order dynamics are conventional, namely curve motion by positive or negative curvature. The correction terms to the dynamics, however, are a mixture of elastic- and surface diffusion-type curve motions. This leads to novel possibilities for circular and other types of equilibrium curves (section 3.3), as well as space-filling pattern proliferation. We illustrate these phenomena and confirm the correctness of our analysis numerically (section 4).

**2. Stripes and their stability.** One-dimensional localized states of (1.1) are obviously also steady states in two dimensions. It is natural to ask whether the stability properties in one dimension also carry forward into two dimensions. This question was addressed numerically by Burke and Knobloch [4] and by Kolokolnikov et al. in the context of the Gierer–Meinhardt model [18]. They found two types of instability: a long-wavelength buckling of the stripe (their unstable "body mode") and a short-wavelength varicose instability (their "wall mode"). The first type of instability more or less preserves the curve-like domain structure (cf. Figure 1(a)). The second type destroys the uniformity of stripe cross sections, and pattern propagation may ensue (cf. Figure 1(b)).

(a) Long-wavelength buckling instability.                    (b) Varicose instability.

**Figure 1.** *Numerical simulation of instabilities of a straight-line domain pattern ($\nu = 4.7$). (a) When $r = -3.9$, the curve is unstable at long wavelengths to sinuous modes that create buckling. (b) When $r = -4.5$, a varicose-type mode is unstable, and the stripe breaks into a series of spots.*

These two types of instability can be quantified analytically. Suppose that there is a one-dimensional localized state $u_0(x)$ satisfying

$$(2.1) \qquad\qquad 0 = -(1 + \partial_x^2)^2 u_0 + N(u_0) + r u_0, \quad -\infty < x < \infty.$$

Such states may in general be stable or unstable (in a one-dimensional sense), since eigenvalues change sign as the snaking bifurcation diagram is traversed. The focus here will be on the former case. The one-dimensional linearized operator

$$(2.2) \qquad\qquad \mathcal{L}_1 \eta \equiv -(1 + \partial_x^2)^2 \eta + [N'(u_0) + r]\eta$$

can be used to determine dynamical behavior in one and two dimensions. Since $u = 0$ is stable in the regime we are interested in, the essential spectrum of $\mathcal{L}_1$ cannot contribute to instability. By virtue of translation invariance, there is a simple eigenvalue at zero with eigenfunction $\eta_0 = \partial_x u_0$. The other eigenvalues of $\mathcal{L}_1$ are real and are presumed stable; the greatest of these will be labeled $\lambda_1 < 0$.
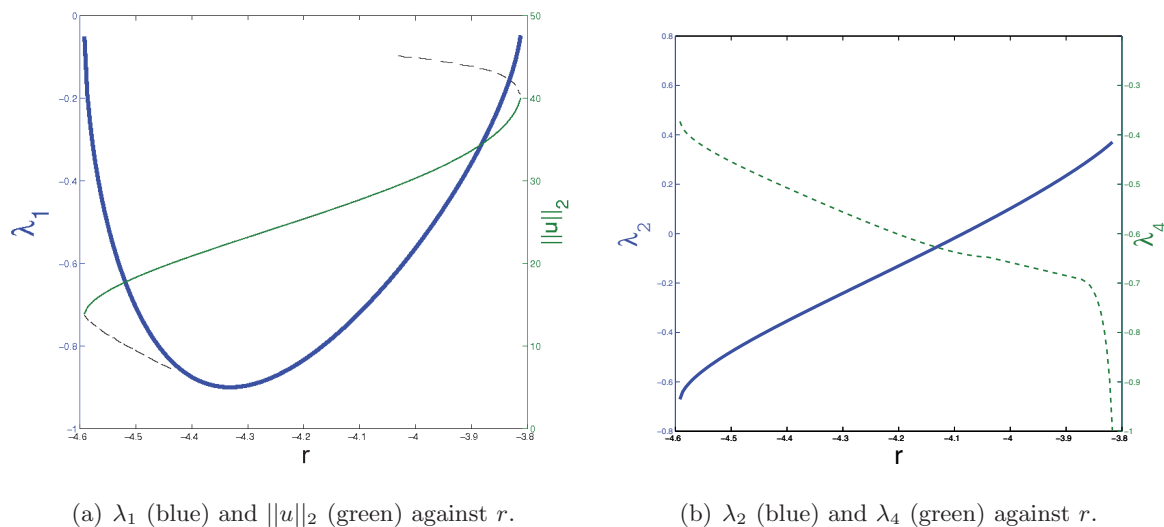
As an example consider the cubic nonlinearity $N(u) = \nu u^2 - u^3$. We have computed the lowest order stable branch of one-dimensional equilibria (for $\nu = 4.7$), together with the principal eigenvalue (Figure 2(a)).

One can regard $u(x, y) = u_0(x)$ as a "partially" localized state in two dimensions, representing a stripe pattern which is infinite in extent in $y$ but localized in the perpendicular direction. Stability can be analyzed using the linearized operator

$$(2.3) \qquad \mathcal{L}\eta \equiv -(1 + \Delta)^2 \eta + [N'(u_0) + r]\eta = \mathcal{L}_1 \eta - 2(1 + \partial_x^2)\partial_y^2 \eta - \partial_y^4 \eta.$$

Consider first modes of the form $\eta = f(y)\chi(x)$, which will be seen to be sinuous perturbations of the straight line domain pattern. Using the Fourier representation

$$(2.4) \qquad\qquad \eta(x, y) = \int_{-\infty}^{\infty} \exp(iky)\hat{\eta}(x, k)dk,$$

(a) $\lambda_1$ (blue) and $\|u\|_2$ (green) against $r$.

(b) $\lambda_2$ (blue) and $\lambda_4$ (green) against $r$.

**Figure 2.** (a) *The bifurcation curve of one-dimensional localized solutions ($N(u) = \nu u^2 - u^3$, $\nu = 4.7$) is represented as the $L_2$ norm squared as a function of the parameter $r$ (thin curves). The dashed part represents the continuation of the solution branch past the saddle nodes at $r \approx -4.6, -3.8$. The principle eigenvalue of the stable branch is also shown (thick/blue curve). (b) The expansion coefficients $\lambda_2$ (solid) and $\lambda_4$ (dashed).*

one can identify a branch $\lambda = \lambda(k), \chi = \chi(x; k)$ of the continuous spectrum, which satisfies

$$(2.5) \qquad \lambda\chi = \mathcal{L}_1\chi + 2k^2(1 + \partial_x^2)\chi - k^4\chi.$$

A perturbation expansion can be used to determine the small $k$ asymptotics, having the form

$$(2.6) \qquad \lambda \sim \lambda_2 k^2 + \lambda_4 k^4 + \cdots, \quad \chi(x; k) \sim \chi_0 + k^2\chi_2 + k^4\chi_4 + \cdots, \quad k \to 0.$$

It is easy to see that the leading term is just the one-dimensional translation eigenfunction $\chi_0 = \eta_0$. At the next order in the expansion,

$$(2.7) \qquad \lambda_2\chi_0 = \mathcal{L}_1\chi_2 + 2(1 + \partial_x^2)\chi_0,$$

whose solvability condition determines the eigenvalue to leading order,

$$(2.8) \qquad \lambda_2 = 2\left[1 - \frac{\langle\eta_{0x}, \eta_{0x}\rangle}{\langle\eta_0, \eta_0\rangle}\right], \qquad \langle u, v\rangle = \int_{-\infty}^{\infty} uv\, dy.$$

To uniquely determine the corrections $\chi_n$, we must stipulate their projection onto the leading order eigenfunction; the simplest way of doing this is just by requiring orthogonality,

$$(2.9) \qquad \langle\eta_0, \chi_n\rangle = 0, \qquad n = 2, 4, 6, \ldots.$$

At the $k^4$ order in the expansion,

$$(2.10) \qquad \lambda_2\chi_2 + \lambda_4\chi_0 = \mathcal{L}_1\chi_4 + 2(1 + \partial_x^2)\chi_2 - \chi_0,$$

whose solvability condition (using (2.9)) is

$$\lambda_4 = \frac{2 \left\langle \eta_0, (1 + \partial_x^2)\chi_2 \right\rangle}{\langle \eta_0, \eta_0 \rangle} - 1. \tag{2.11}$$

An assessment of the signs of $\lambda_2$ and $\lambda_4$ is useful. The expression for $\lambda_2$ in (2.8) will be shown to arise naturally from a variational argument as a "line" energy, and it can be either negative or positive (cf. Figure 2(b)). The expression for $\lambda_4$ can be simplified by taking the inner product of (2.7) with $\chi_2$, to give

$$\lambda_4 = \frac{- \left\langle \chi_2, \mathcal{L}_1 \chi_2 \right\rangle}{\langle \eta_0, \eta_0 \rangle} - 1. \tag{2.12}$$

Note that by assuming the one-dimensional stability of $u_0$ and orthogonality of $\chi_2$ and $\eta_0$, it follows that

$$\langle \chi_2, \mathcal{L}_1 \chi_2 \rangle < 0. \tag{2.13}$$

One obtains from (2.12) and (2.13) the lower bound $\lambda_4 > -1$. On the other hand, numerical solution seems to indicate that $\lambda_4$ is generally negative (cf. Figure 2(b)).

There are two scenarios that may be extracted from this analysis. If $\lambda_2 < 0$, then long-wavelength sinuous perturbations do not grow. On the other hand, if $\lambda_2 > 0$ and $\lambda_4 < 0$, then a finite wavelength "buckling" instability occurs.

The more general eigenvalue problem with $\hat{\eta} = \hat{\eta}(x, k)$ can be written in Fourier variables as

$$\lambda \hat{\eta} = \mathcal{L}_1 \hat{\eta} + 2k^2(1 + \partial_x^2)\hat{\eta} - k^4 \hat{\eta} \equiv \hat{\mathcal{L}} \hat{\eta}. \tag{2.14}$$

Suppose now that $\hat{\eta}$ is orthogonal to the modes considered above, in the one-dimensional sense

$$\langle \hat{\eta}(x, k), \eta_0(x) \rangle = 0. \tag{2.15}$$

An estimate on the remaining eigenvalues can be made by considering the Rayleigh quotient. In particular, if the normalization condition $\int_{-\infty}^{\infty} \int_{-\infty}^{\infty} \hat{\eta}^2 \, dx dk = 1$ holds,

$$\begin{aligned}
\lambda &\leq \int_{-\infty}^{\infty} \int_{-\infty}^{\infty} \hat{\eta} \hat{\mathcal{L}} \hat{\eta} \ dx dk \\
&= \int_{-\infty}^{\infty} \int_{-\infty}^{\infty} \hat{\eta} L_0 \hat{\eta} - 2k^2 \hat{\eta}_x^2 \ dx dk + 2k^2 - k^4 \\
&\leq \lambda_1 + 2k^2 - k^4,
\end{aligned} \tag{2.16}$$

where the second inequality results from the one-dimensional variational estimate

$$\langle \hat{\eta}, L_0 \hat{\eta} \rangle \leq \lambda_1 \langle \hat{\eta}, \hat{\eta} \rangle, \tag{2.17}$$

assuming that $\hat{\eta}$ is orthogonal to $\eta_0$ in the sense of (2.15).

The stripe therefore can evolve in two ways: either by preserving its cross section and undergoing a sinuous motion, or more generally by breaking into a patterned state that varies along the stripe, destroying the uniformity of cross sections. A sufficient criteria to prevent the latter from occurring can be derived from (2.16) by insisting that the largest nontrivial eigenvalue be negative enough so that

$$(2.18) \qquad \lambda_1 \leq \inf_k(-2k^2 + k^4) = -1.$$

In other words, if the cross section is stable enough in the one-dimensional sense, then one would expect the domain to evolve as a curved domain of roughly constant cross section. In the next section, the evolution of these curved domains is analyzed.

**3. Evolution of curved domains.** In this section, the dynamics of curved filaments in the rescaled equation

$$(3.1) \qquad \epsilon^2 u_t = ru - (1 + \epsilon^2 \Delta)^2 u + N(u)$$

are analyzed in the limit $\epsilon \to 0$. The analysis follows through for general nonlinearity $N(u)$, which is left unspecified for now. In this particular limit, the evolution of spatially localized one-dimensional filaments under (3.1) is considered. More precisely, we investigate the dynamics of the curve $\Gamma(x, t; \epsilon) = 0$, which is concurrent with the global maximum of a one-dimensional equilibrium profile of (3.1) extending normally to $\Gamma = 0$ and exhibiting exponential decay to 0 in the far field.

The analysis is facilitated by employing a fitted orthogonal system $(\rho(x, t; \epsilon), s(x, t; \epsilon))$ [12], where the coordinate $\rho$ designates the signed perpendicular distance from the centerline $\Gamma = 0$ of the filament, while $s$ denotes, for $x \in \Gamma$, the arc-length along it. In this coordinate system, we have that

$$\Delta \equiv \frac{\partial^2}{\partial \rho^2} - \frac{\kappa}{1 - \kappa\rho}\frac{\partial}{\partial \rho} + \frac{1}{1 - \kappa\rho}\frac{\partial}{\partial s}\left(\frac{1}{1 - \kappa\rho}\frac{\partial}{\partial s}\right),$$

where $\kappa \equiv \kappa(s)$ is the curvature of $\Gamma$. This implies a sign convention for curvature, namely that $\kappa > 0$ if the set $\{\rho > 0\}$ is locally convex.

In the vicinity of the centerline, a local rescaling of solutions

$$u(x, t; \epsilon) = v(z, s, t; \epsilon), \qquad z(x, t; \epsilon) = \rho(x, t; \epsilon)/\epsilon$$

is implemented so that (3.1) becomes
(3.2)
$$\epsilon^2\left(v_t + \frac{\rho_t}{\epsilon}v_z + v_s s_t\right) = rv - \left[1 + \frac{\partial^2}{\partial z^2} - \frac{\epsilon\kappa}{1 - \epsilon\kappa z}\frac{\partial}{\partial z} + \frac{\epsilon^2}{1 - \epsilon\kappa z}\frac{\partial}{\partial s}\left(\frac{1}{1 - \epsilon\kappa z}\frac{\partial}{\partial s}\right)\right]^2 v + N(v).$$

Further expanding with
(3.3)
$$v(z, s, t; \epsilon) = v_0(z) + \epsilon v_1(z, s, t) + \epsilon^2 v_2(z, s, t) + \cdots, \qquad \rho = \rho_0(s, t) + \epsilon\rho_1(s, t) + \epsilon^2\rho_2(s, t) + \cdots$$

and collecting terms at various orders results in a sequence of problems to be analyzed. Before proceeding with the detailed calculation of this perturbed solution, we also remark that an

additional condition is required to uniquely specify the centerline of the perturbed solution. A natural choice dictates that the projection of the null vector $\eta_0$ (cf. (2.7)) onto the solution should be zero, i.e., that

$$\text{(3.4)} \qquad \langle \eta_0, v \rangle = \int_{-\infty}^{\infty} \eta_0 v \, dz = 0.$$

This condition is crucial in ensuring that the perturbed solution $v$ of (3.3) and the centerline $\Gamma$ is uniquely defined. We now proceed by substituting (3.3) into (3.2) and collecting terms at each order.

*Order $\epsilon^0$.* At leading order, $v_0(z)$ satisfies the base equation

$$\text{(3.5)} \qquad r \, v_0 - \left( 1 + \frac{\partial^2}{\partial z^2} \right)^2 v_0 + N(v_0) = 0, \qquad z \in \mathbb{R}, \qquad v_0 \to 0, \quad |z| \to \infty.$$

*Order $\epsilon$.* At the following order, the equation

$$\text{(3.6)} \qquad \mathcal{L} v_1 = v_{0z} \rho_{0t} - 2\kappa(v_{0z} + v_{0zzz})$$

is obtained, where the self-adjoint linear differential operator $\mathcal{L}$ is defined to be

$$\text{(3.7)} \qquad \mathcal{L} \equiv r - \left( 1 + \frac{\partial^2}{\partial z^2} \right)^2 + N'(v_0).$$

A differentiation of (3.5) with respect to $z$ reveals that $\mathcal{L} v_{0z} = 0$, and so $\mathcal{L}$ has a nontrivial null space, corresponding to the translation invariance of (3.5). Note that the quantity $v_{0z}$ is exactly $\eta_0$, obtained from (2.7). Accordingly, (3.6) has a solution only when its right-hand side is orthogonal to $v_{0z}$, i.e., when

$$\text{(3.8)} \qquad \langle v_{0z} \rho_{0t} - 2\kappa(v_{0z} + v_{0zzz}), v_{0z} \rangle = 0, \qquad \langle u, v \rangle = \int_{-\infty}^{\infty} uv \, dy.$$

Rearranging this solvability condition gives the leading order normal velocity,

$$\text{(3.9)} \qquad \rho_{0t} = 2\kappa \left( 1 - \frac{\langle v_{0zz}, v_{0zz} \rangle}{\langle v_{0z}, v_{0z} \rangle} \right).$$

Consequently, (3.8) for $v_1$ is reduced to

$$\text{(3.10)} \qquad \mathcal{L} v_1 = -2\kappa \left( v_{0zzz} + v_{0z} \frac{\langle v_{0zz}, v_{0zz} \rangle}{\langle v_{0z}, v_{0z} \rangle} \right).$$

*Order $\epsilon^2$.* At the next order, $v_2$ is found to satisfy

$$\text{(3.11)} \quad \mathcal{L} v_2 = -\kappa^2 \big( v_{0zz} + 2z(v_{0z} + z v_{0zzz}) \big) - 2\kappa(v_{1z} + v_{1zzz}) + v_{0z} \rho_{1t} + v_{1z} \rho_{0t} - \frac{v_1^2}{2} N''(v_0),$$

and again we enforce that the right-hand side of (3.11) be orthogonal to $v_{0z}$. As $v_0(z)$ and $v_1(z)$ are even and odd functions about $z = 0$, respectively, several components of the solvability

condition integrate to zero, leaving the reduced condition $\rho_{1t}\langle v_{0z}, v_{0z}\rangle = 0$. Consequently there is no contribution to the normal motion of the centerline at this order, and (3.11) reduces to

$$(3.12) \qquad \mathcal{L}v_2 = -\kappa^2\big(v_{0zz} + 2z(v_{0z} + v_{0zzz})\big) - 2\kappa\left(v_{1zzz} + v_{1z}\frac{\langle v_{0zz}, v_{0zz}\rangle}{\langle v_{0z}, v_{0z}\rangle}\right) - \frac{v_1^2}{2}N''(v_0).$$

*Order $\epsilon^3$.* At the subsequent order, the equation for $v_3$ is determined to be

$$\mathcal{L}v_3 = -2\kappa^3\left(zv_{0zz} + z^2 v_{0zzz} + \frac{1}{2}v_{0z} + z^2 v_{0z}\right) - \kappa^2\big(v_{1zz} + 2z(v_{1z} + v_{1zzz})\big) - \kappa_{ss}v_{0z}$$

$$- 2\kappa\left(v_{2zzz} + v_{2z}\frac{\langle v_{0zz}, v_{0zz}\rangle}{\langle v_{0z}, v_{0z}\rangle}\right) + 2(v_{1sszz} + v_{1ss}) + \rho_{2t}v_{0z} + v_1 v_2 N''(v_0)$$

$$(3.13) \qquad + \frac{v_1^3}{6}N'''(v_0) + v_{1s}s_t + v_{1t}.$$

Before applying the solvability condition to (3.13), let us first consider the following simplification afforded by a consideration of the differential operator:

$$\tilde{D} \equiv \frac{\partial}{\partial t} + s_t\frac{\partial}{\partial s}.$$

By introducing the temporary function $s = S(X(s,t), t)$, where $s$ and $t$ are independent variables, we have that

$$0 = \nabla_x S(X, t) \cdot \frac{\partial}{\partial t}X + \frac{\partial}{\partial t}S(X, t).$$

Consequently $\tilde{D}v_1(z, s) = \tilde{D}v_1(z, S(X, t)) = 0$, and so (3.13) reduces to

$$\mathcal{L}v_3 = -2\kappa^3\left(zv_{0zz} + z^2 v_{0zzz} + \frac{1}{2}v_{0z} + z^2 v_{0z}\right) - \kappa^2\big(v_{1zz} + 2z(v_{1z} + v_{1zzz})\big) - \kappa_{ss}v_{0z}$$

$$(3.14) \quad - 2\kappa\left(v_{2zzz} + v_{2z}\frac{\langle v_{0zz}, v_{0zz}\rangle}{\langle v_{0z}, v_{0z}\rangle}\right) + 2(v_{1sszz} + v_{1ss}) + \rho_{2t}v_{0z} + v_1 v_2 N''(v_0) + \frac{v_1^3}{6}N'''(v_0).$$

Unique solutions $v_1$ and $v_2$ for (3.10) and (3.13) are obtained by applying the constraints $\langle v_1, v_{0z}\rangle = \langle v_2, v_{0z}\rangle = 0$, and consequently we obtain that
$$(3.15)$$
$$v_1(s, z) = \kappa\bar{v}_1 = \kappa\left(\bar{v}_{1p} - v_{0z}\frac{\langle\bar{v}_{1p}, v_{0z}\rangle}{\langle v_{0z}, v_{0z}\rangle}\right), \quad v_2(s, z) = \kappa^2\bar{v}_2 = \kappa^2\left(\bar{v}_{2p} - v_{0z}\frac{\langle\bar{v}_{2p}, v_{0z}\rangle}{\langle v_{0z}, v_{0z}\rangle}\right).$$

In the above expressions, $\bar{v}_{1p}(z)$ and $\bar{v}_{2p}(z)$ solve the associated problems

$$(3.16) \qquad \mathcal{L}\bar{v}_{1p} = -2\left(v_{0zzz} + v_{0z}\frac{\langle v_{0zz}, v_{0zz}\rangle}{\langle v_{0z}, v_{0z}\rangle}\right),$$

$$(3.17) \qquad \mathcal{L}\bar{v}_{2p} = -\big(v_{0zz} + 2z(v_{0z} + v_{0zzz})\big) - 2\left(\bar{v}_{1zzz} + \bar{v}_{1z}\frac{\langle v_{0zz}, v_{0zz}\rangle}{\langle v_{0z}, v_{0z}\rangle}\right) - \frac{\bar{v}_1^2}{2}N''(v_0).$$

Applying the solvability condition $\langle \mathcal{L}v_3, v_{0z} \rangle = 0$ to (3.14), the correction to the normal motion of the centerline is found to be

$$(3.18) \qquad \rho_{2t} = \alpha_1 \kappa_{ss} + \alpha_2 \kappa^3$$

for constants $\alpha_1$, $\alpha_2$ whose values are certain inner products in terms of known quantities:

$$(3.19)$$

$$\alpha_1 = 1 - 2\frac{\langle \bar{v}_{1zz} + \bar{v}_1, v_{0z} \rangle}{\langle v_{0z}, v_{0z} \rangle} = 1 - 2\frac{\langle \bar{v}_{1zz}, v_{0z} \rangle}{\langle v_{0z}, v_{0z} \rangle},$$

$$\alpha_2 = \frac{1}{\langle v_{0z}, v_{0z} \rangle}\left[\left\langle 2\left(zv_{0zz} + z^2 v_{0zzz} + \frac{1}{2}v_{0z} + z^2 v_{0z}\right) + \left(\bar{v}_{1zz} + 2z(\bar{v}_{1z} + \bar{v}_{1zzz})\right), v_{0z}\right\rangle\right]$$

$$+ \frac{1}{\langle v_{0z}, v_{0z} \rangle}\left[\left\langle 2\left(\bar{v}_{2zzz} + \bar{v}_{2z}\frac{\langle v_{0zz}, v_{0zz} \rangle}{\langle v_{0z}, v_{0z} \rangle}\right) - \bar{v}_1\bar{v}_2 N''(v_0) - \frac{\bar{v}_1^3}{6}N'''(v_0), v_{0z}\right\rangle\right].$$

Finally, the normal velocity of the centerline is found to obey the following asymptotic differential equation:

$$(3.20) \qquad \frac{\partial \rho}{\partial t} \sim 2\kappa\left(1 - \frac{\langle v_{0zz}, v_{0zz} \rangle}{\langle v_{0z}, v_{0z} \rangle}\right) + \epsilon^2\left(\alpha_1 \kappa_{ss} + \alpha_2 \kappa^3\right) + \cdots.$$

This expression is valid for $\kappa = \mathcal{O}(1)$, i.e., provided the curved domain does not become too contorted. Note that the coefficient of the $\kappa$ term is identical to $\lambda_2$, derived in (2.8).

**3.1. Relationship of curve motion to stripe stability and a variational interpretation.**
To reinforce the validity of the foregoing calculation, we compare it to the calculation of stripe stability. A nearly straight curve can be parameterized by its centerline displacement $h(s)$. With the sign conventions for curvature and normal velocity above, the linearized motion (with larger $h(s)$ in the direction of positive $\rho$ so that $h_{ss}$ is linearized curvature) reads

$$(3.21) \qquad h_t = \gamma h_{ss} - \epsilon^2 \alpha_1 h_{ssss}, \quad \gamma = 2\left(\frac{\langle v_{0zz}, v_{0zz} \rangle}{\langle v_{0z}, v_{0z} \rangle} - 1\right).$$

The real growth rate of a Fourier mode $\exp(ikx)$ is $-\gamma k^2 - \epsilon^2 \alpha_1 k^4$. Note that the scaled correction term $\bar{v}_1$ solves (3.6), which is the same equation satisfied by $\chi_2$ in the eigenvalue perturbation expansion (equation (2.7)). It is then easy to check that $\lambda_2 = -\gamma$ and $\lambda_4 = -\alpha_1$. In other words, the stability calculation is recovered from the asymptotic curve motion.

We can further note that the leading order dynamics are variational, namely, the gradient flow of a curve whose energy per unit length is $\gamma$. We can see how $\gamma$ arises from the energy of the Swift–Hohenberg equation,

$$(3.22) \qquad E = \int \frac{1}{2}[(1+\Delta)u]^2 + g(u)\, dx, \quad g'(u) = ru - N(u).$$

In scaled variables, the cross-sectional energy of a curve is

$$(3.23) \qquad E_{cross} = \int \frac{1}{2}[(1+\partial_z^2)v_0]^2 + g(v_0)\, dz.$$

Equation (3.5) for $v_0$ admits a first integral by multiplying by $v_{0z}$ and integrating,

$$\text{(3.24)} \qquad \frac{1}{2}v_0^2 + v_{0z}^2 - \frac{1}{2}v_{0zz}^2 + v_{0zzz}v_{0z} + g(v_0) = 0.$$

This expression allows $g(v_0)$ to be written in terms of derivatives; inserting into (3.23) and integrating by parts gives

$$\text{(3.25)} \qquad E_{cross} = 2\int v_{0zz}^2 - v_{0z}^2 \, dz = \gamma.$$

**3.2. Curve lengthening and regularization of the dynamics.** When $\gamma > 0$, the leading order dynamics are standard motion by mean curvature, whose properties are well documented (e.g., [11]). In contrast, $\gamma < 0$ gives an ill-posed curve evolution at leading order. This justifies the necessity of correction terms which might regularize the curve motion equations.

The two-order composite evolution (3.20) may be decomposed into three well-studied intrinsic curve motions: motion by curvature, elastic curve motion, and motion by the Laplacian of curvature, also called surface diffusion. In particular, one can write the correction to the curve velocity as

$$\text{(3.26)} \qquad \alpha_1\kappa_{ss} + \alpha_2\kappa^3 = 2\alpha_2 V_e + (\alpha_1 - 2\alpha_2)V_{sd}.$$

The elastic motion law $V_e = \kappa_{ss} + \frac{1}{2}\kappa^3$ arises as a gradient flow of the curve energy,

$$\text{(3.27)} \qquad E_e = \frac{1}{2}\int_\Gamma \kappa^2 \, ds,$$

and has been studied as a regularization of ill-posed curvature flows [5]. The $\mathcal{O}(\epsilon^2)$ evolution equation (3.20) reduces to this case if $\alpha_1 = 2\alpha_2$. The surface diffusion velocity contribution $V_{sd} \sim \kappa_{ss}$ is also used as a regularization of curvature dependent motions (see [20] and references therein).

The fact that the line energy coefficient $\gamma$ can have either sign means that curves may either lengthen or shorten at leading order. If $\Gamma$ is a closed curve evolving under (3.20), a standard calculation for the length of the curve $L(t)$ reveals that

$$\text{(3.28)} \qquad \frac{dL}{dt} = \int_\Gamma \kappa\frac{\partial\rho}{\partial t} \, ds = -\gamma\int_\Gamma \kappa^2 \, ds + \alpha_2\epsilon^2\int_\Gamma \kappa^4 \, ds - \epsilon^2\alpha_1\int_\Gamma \kappa_s^2 \, ds.$$

The qualitative effect of the coefficients is clear. If $\gamma > 0$, usual curvature flow makes the curve shrink. On the other hand, if $\gamma < 0$, the curve will generally buckle and proliferate, until the curvature gradients become large enough to arrest curve lengthening.

If $\gamma = \mathcal{O}(1)$, then the potential growth-arresting effects of the surface diffusion term will only be felt when gradients of curvature are appreciable on a length scale of $\mathcal{O}(\epsilon)$. While this poses no difficulty for the sharp interface dynamics, it is unlikely that the asymptotic analysis would be valid if the curved domain was undulating on a scale comparable to its width.

(a) $r = -4.2$, $\gamma \approx 0.1320$.  (b) $r = -3.9$, $\gamma \approx -0.2335$.
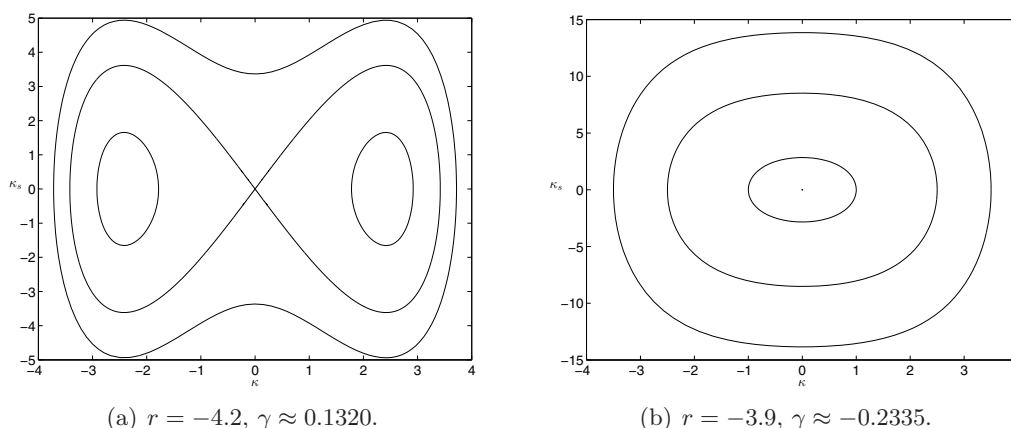
**Figure 3.** *Typical phase plane diagrams associated with system* (3.29) *for* $\epsilon = 0.2$, $\nu = 4.7$. (a) *Curves for* $\gamma > 0$. *The center curve is a homoclinic orbit, and the remaining two curves are periodic orbits of large and small amplitude.* (b) *Curves for* $\gamma < 0$. *The origin is a center, and all other trajectories are periodic orbits.*

### 3.3. Circular, meandering, and self-intersecting steady state curves.

In this section, we investigate the equilibrium structure of (3.20) by considering all solutions of the system

$$(3.29) \qquad -\gamma\kappa + \epsilon^2\Big(\alpha_1\kappa_{ss} + \alpha_2\kappa^3\Big) = 0,$$

along with the planar curves which they generate. To obtain values for the parameters $\gamma, \alpha_1$, and $\alpha_2$, we focus on the quadratic-cubic nonlinearity $N(u) = \nu u^2 - u^3$ case. The aforementioned quantities are then calculated by first obtaining the solution of the one-dimensional equilibrium problem,

$$(3.30) \qquad r\,v - \left(1 + \frac{d^2}{dz^2}\right)^2 v + \nu\,v^2 - v^3 = 0, \qquad z \in \mathbb{R}; \qquad v \to 0, \quad |z| \to \infty.$$

A numerical solution of (3.30) is obtained from a spatial discretization based on a finite difference approximation on a large but finite region. An appropriate initial profile is provided, followed by Newton iterations until a specified tolerance is obtained. The quantities required for (3.29) are then readily obtained from quadrature of this numerical approximation.

Continuing on with our analysis of (3.29), we observe the Hamiltonian

$$(3.31) \qquad H = \epsilon^2\frac{\alpha_1}{2}\kappa_s^2 + \epsilon^2\frac{\alpha_2}{4}\kappa^4 - \frac{\gamma}{2}\kappa^2.$$

A similar steady state equation of curve motion was considered by Gavish et al. [13] in a completely different model that forms narrow domains. Let us consider the cases $\gamma > 0$ and $\gamma < 0$ separately.

*Case $\gamma > 0$.* A phase plane analysis of (3.31) (if $\alpha_1 > 0, \alpha_2 > 0, \gamma > 0$) reveals a homoclinic, large-amplitude (i.e., large $H$), and small-amplitude orbits (cf. Figure 3(a) for typical solutions). The curves $\Gamma(s) = (x(s), y(s))$ associated with these equilibrium solutions

(a) Non–self-intersecting curves, $r = -4.2$.  (b) Self-intersecting curves, $r = -4.4$.
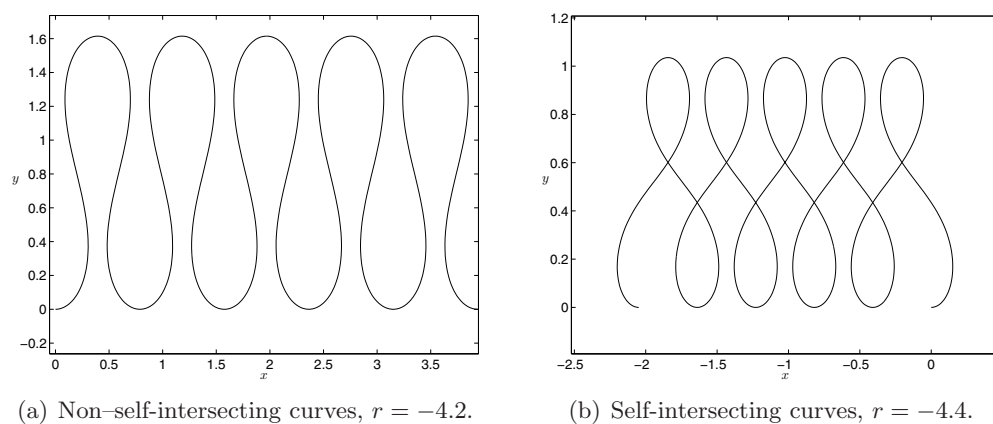
**Figure 4.** *Planar curves associated with large-amplitude solutions of* (3.29). *Both plots share the values* $\epsilon = 0.2$ *and* $\nu = 4.7$. (a) *shows non–self-intersecting curves arising from the parameter value* $r = -4.2$, *while* (b) *shows self-intersecting curves arising from* $r = -4.4$.

$\kappa(s)$ of (3.29) can be reconstructed by solving the system

$$(3.32) \qquad \begin{bmatrix} \theta(s) \\ x(s) \\ y(s) \end{bmatrix}_s = \begin{bmatrix} \kappa(s) \\ \cos\theta(s) \\ \sin\theta(s) \end{bmatrix},$$

where $\theta(s)$ indicates the angle made by the tangent of $\Gamma$ at $s$ with the horizontal. From this, the large-amplitude periodic orbits of (3.29) are found (cf. Figure 4) to describe meandering curves, which can be either self- or non–self-intersecting.

These meandering curves, arising from large-amplitude orbits of (3.29), are not closed, however. The question of which functions $\kappa(s)$ give rise to closed curves in $\mathbb{R}^2$ is a classic problem in planar geometry. In particular (cf. [1]), if $\kappa(s)$ is periodic with minimal period $\rho_\kappa$, then the curve $\Gamma_\kappa$ whose curvature is $\kappa$ closes up in $[0, n\rho_\kappa]$, $n > 1$, if and only if there exists an integer $m$ such that

$$(3.33) \qquad \frac{1}{2\pi} \int_0^{\rho_\kappa} \kappa(s)\, ds = \frac{m}{n}.$$

From the phase plane of (3.29), shown in Figure 3, the symmetry of large-amplitude orbits implies that

$$\int_0^{\rho_\kappa} \kappa(s)\, ds = 0,$$

and consequently these orbits will never generate closed planar curves. The small-amplitude orbits seen inside the homoclinic of Figure 3(a) do have nonzero values of $\int_0^{\rho_\kappa} \kappa(s)\, ds$. Indeed, for given $m$ and $n$ it is possible to locate appropriate initial conditions and consequently trajectories which satisfy condition (3.33). However, the closed curves found (cf. Figure 5) appear to be exclusively self-intersecting.

It is also possible to have steady state circular solutions, whose radii satisfy $R_0 = \kappa_0^{-1} = \epsilon\sqrt{\alpha_2/\gamma}$, provided that $\alpha_2$ and $\gamma$ have the same sign. The linearized stability of these equilibria is straightforward to compute. (Note that the dynamics in [13] are different from ours;

(a) Closed curve, $r = -4.187$.     (b) Closed curve, $r = -4.1085$.
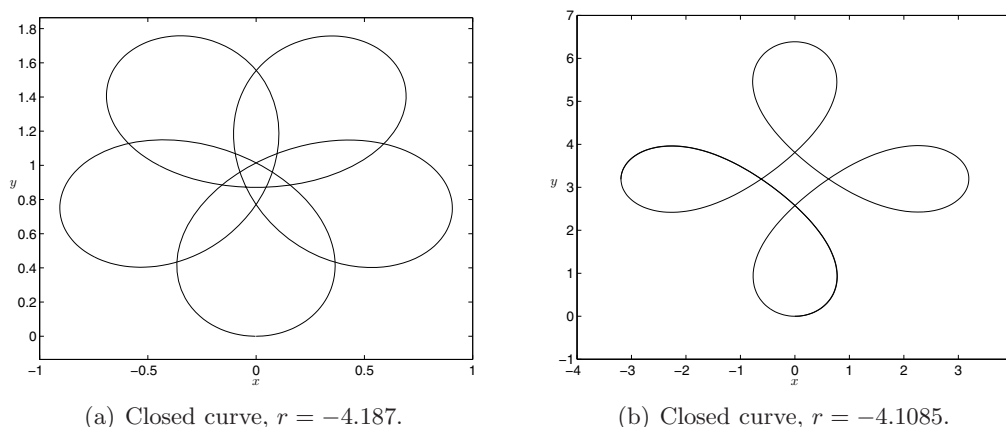
**Figure 5.** *Two examples of closed intersecting curves generated from orbits of* (3.29). *Parameter values for both figures:* $\epsilon = 0.2$, $\nu = 4.7$.

in particular, the arc-length here is not conserved.) Suppose first that $\gamma, \alpha_2 > 0$, and nondimensionalize by rescaling lengths by $R_0$ and time by $R_0/\gamma$, so that the normal velocity is

$$(3.34) \qquad V_n = \mu\, \kappa_{ss} + \kappa^3 - \kappa, \qquad \mu \equiv \frac{\alpha_1}{\alpha_2}.$$

Consider the evolution of a normal perturbation $v(s,t)$ so that the curve is parameterized as $(x(s), y(s)) = (1 + v)[\cos(s), \sin(s)]$ for $0 \le s < 2\pi$. The curvature expands as $\kappa = 1 - v_{ss} - v + \mathcal{O}(v^2)$, so that the linearized dynamics correspond to

$$(3.35) \qquad v_t = -\mu\, v_{ssss} - (\mu + 2)v_{ss} - 2v.$$

The growth rate $\sigma$ of modes $\exp(ins)$, $n = 0, 1, 2, \ldots$, is therefore

$$(3.36) \qquad \sigma_n = -\mu\, n^4 + (\mu + 2)n^2 - 2.$$

The uniform translation mode $n = 1$ naturally gives $\sigma_1 = 0$. It is not difficult to see that if instability occurs, then the second mode's growth rate $\sigma_2 = -12\mu + 6$ must be positive. This occurs when $\mu < \frac{1}{2}$. This means that if surface diffusion effects (given by the coefficient $\alpha_1$) are large enough, circular equilibria will be stable.

*Case $\gamma < 0$.* In this case, the origin is a center, and all trajectories are periodic orbits, as seen in Figure 3(b). As each of these orbits satisfies $\int_0^{\rho_\kappa} \kappa(s)\, ds = 0$, they do not generate closed planar curves but instead sinusoidal nonintersecting curves.

The previous phase plane analysis indicates that a closed curve, evolving under the dynamics predicted by (3.20), can equilibrate to circles in the case $\gamma > 0$. All other closed curves generated by solutions of (3.29) are self-intersecting. We do find meandering, non–self-intersecting equilibrium curves (cf. Figure 4(a)), which correspond to large-amplitude periodic orbits of (3.29).

**4. Full two-dimensional numerical tests.** In this section, we investigate the qualitative predictions of (3.20), in particular the centerline dynamics of

$$(4.1) \qquad \frac{\partial \rho}{\partial t} \sim -\gamma \kappa + \epsilon^2 \Big( \alpha_1 \kappa_{ss} + \alpha_2 \kappa^3 \Big) + \cdots, \qquad \gamma = 2 \left( \frac{\langle v_{zz}, v_{zz} \rangle}{\langle v_z, v_z \rangle} - 1 \right),$$

by means of comparison with full numerical simulations of (3.1). The full two-dimensional simulations of (3.1) are performed on the square region $\Omega = [-10, 10]^2$ with Fourier decomposition in space and adaptive time stepping. Along the boundary of the region, the solution and its normal derivative are required to be zero.

Numerical simulation of the interfacial equation (4.1) is achieved with the level set methods described in [7, 29], which we now briefly summarize. This approach represents the interface $\Gamma$ as the zero level set of a function $\phi(x, y, t)$, i.e., $\Gamma = \{(x, y) \mid \phi(x, y, t) = 0\}$. Differentiating the expression $\phi(x, y, t) = 0$ implicitly with respect to $t$ gives $\phi_t + \rho_t |\nabla \phi| = 0$, where $\rho_t$ is the normal velocity given in (4.1). Consequently, we consider the equation

$$(4.2) \qquad \phi_t + \big[ -\gamma \kappa + \epsilon^2 (\alpha_1 \kappa_{ss} + \alpha_2 \kappa^3) \big] |\nabla \phi| = 0,$$

which is simulated by discretization on a uniform Cartesian grid via second order centered differences. The appropriate formulas for $\kappa$ and $\kappa_{ss}$ in this coordinate system are given (cf. [29]) by

$$(4.3\text{a}) \qquad \kappa = \frac{\phi_{xx} \phi_y^2 - 2 \phi_{xy} \phi_x \phi_y + \phi_{yy} \phi_x^2}{\phi_x^2 + \phi_y^2},$$
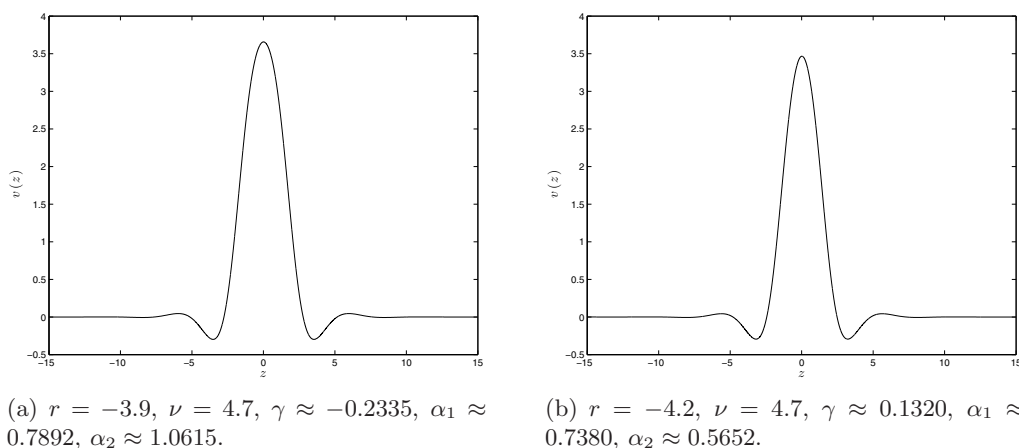
$$(4.3\text{b}) \qquad \kappa_{ss} = \frac{\kappa_{xx} \phi_y^2 - 2 \kappa_{xy} \phi_x \phi_y + \kappa_{yy} \phi_x^2}{\phi_x^2 + \phi_y^2} - \frac{\kappa (\kappa_x \phi_x + \kappa_y \phi_y)}{(\phi_x^2 + \phi_y^2)^{1/2}}.$$

After discretization, the system obtained for the unknowns is of form $\phi_t = S(\phi)$, where $S(\phi)$ is nonlinear, fourth order, and prone to instability when evolved. An explicit integration scheme suffers from a very severe CFL condition, while implicit schemes are of limited feasibility for such a nonlinear equation. The semi-implicit scheme employed in [29] is one way to bypass some of these difficulties. We first write $\phi_t = -\beta \Delta^2 \phi + (\beta \Delta^2 \phi + S(\phi))$ and treat the first term implicitly and the second explicitly. This results in the first order accurate iteration scheme

$$(4.4) \qquad \phi^{n+1} = \phi^n + \big[ 1 + \Delta t \beta \Delta^2 \big]^{-1} \big[ \Delta t S(\phi^n) \big]$$

for a fixed time step $\Delta t$. The effect of the nonlocal operator $[1 + \Delta t \beta \Delta^2]^{-1}$ is to stabilize the otherwise explicit scheme. In our simulations, we use the value $\beta = 1/2$ and invert the fourth order operator with an FFT. To reduce unnecessary computational work, the system is evolved only in a thin band of mesh points surrounding the interface, and the values of the quantities (4.3) on the interface are extended normally to those points.

In the following examples, we illustrate the dynamics of two-dimensional structures under (3.1) where those structures are constructed from two particular one-dimensional cross-sectional profiles, each having a $\gamma$ value of differing sign. The two cross-sectional profiles considered are shown in Figure 6 and appear to be qualitatively identical. However, when

(a) $r = -3.9$, $\nu = 4.7$, $\gamma \approx -0.2335$, $\alpha_1 \approx 0.7892$, $\alpha_2 \approx 1.0615$.

(b) $r = -4.2$, $\nu = 4.7$, $\gamma \approx 0.1320$, $\alpha_1 \approx 0.7380$, $\alpha_2 \approx 0.5652$.

**Figure 6.** *Two one-dimensional cross-sectional solutions of* (3.30) *used to generate a spatially localized two-dimensional solution. Each profile results in a value of $\gamma$ of differing sign, and consequently each will result in different qualitative behavior arising from* (3.20).

two-dimensional filaments are constructed by taking these profiles as cross sections, very different qualitative dynamics emerge, as predicted by the previous steady state analysis of (4.1). Numerical simulations of the interface equation (4.1) are also compared with those of (3.1), and qualitative agreement is observed. The self-interaction of the curve with its distal segments is observed to be very important in the evolution of the domain. The geometric evolution (4.1) does not account for these interactions and indeed allows for self-intersection which is not observed in full numerical solutions of (3.1). Consequently, quantitative predictions from the full two-dimensional asymptotic theory are found to be less good, particularly in the curve lengthening case. However, in the radially symmetric case, good quantitative agreement is obtained.

**4.1. Example 1: Curve lengthening and space filling.** Here the values $r = -3.9$, $\nu = 4.7$, and $\epsilon = 0.2$ are used to initialize two-dimensional simulations of (3.1) in the square region $[-10, 10]^2$. The corresponding values in the reduced asymptotic theory, calculated from (3.19), are $\gamma \approx -0.2335$, $\alpha_1 \approx 0.7892$, and $\alpha_2 = 1.0615$. The initial data is nonzero except in a region of width $\epsilon$ centered on the ellipse $1.5\, x^2 + y^2 = 9$. In the direction transverse to the ellipse, the numerical solution of (3.1) quickly stabilizes to the one-dimensional solution profile of (3.30) shown in Figure 6(a). The resulting two-dimensional structure is stable, as predicted by the results of section 2. To leading order, (4.1) predicts centerline dynamics $\rho_t \approx -\gamma\kappa$, where $\gamma \approx -0.2335$, and the order $\mathcal{O}(\epsilon^2)$ terms provide a regularization to this ill-posed motion. Accordingly, inhomogeneities in the initial data are accentuated by the dynamics, and the curve lengthens and buckles as predicted in section 3.2.

In full two-dimensional simulations of (3.1), self-intersection eventually becomes a possibility but is prevented by repulsive forces generated by the interaction of the exponential tails emanating from distal parts of the curve (cf. section 4.3). As demonstrated in the phase plane analysis of section 3.3 for the case $\gamma < 0$, the dynamics of (4.1) alone will not equilibrate curve motion. Consequently, the curved domain will continue to buckle and lengthen
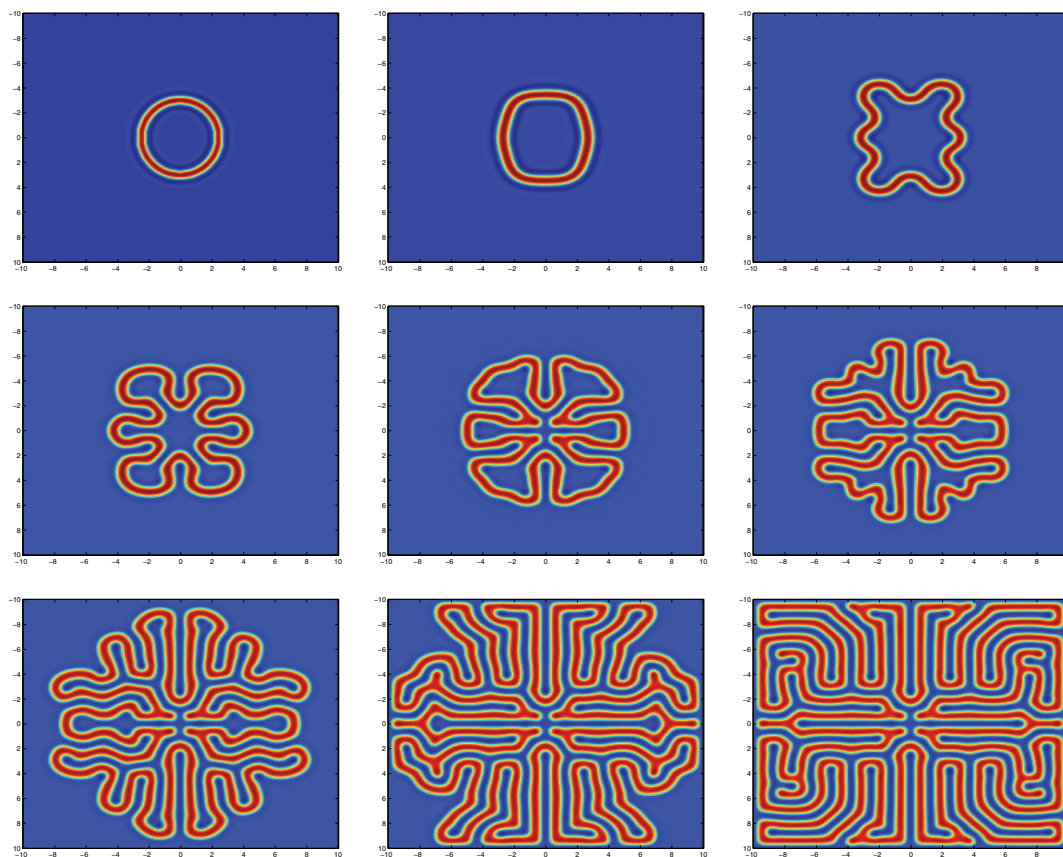
**Figure 7.** *Evolution of* (3.1) *with nonzero initial data provided on a region of width $\epsilon$ centered around the ellipse $1.5\,x^2 + y^2 = 9$. The parameter values $\epsilon = 0.2$, $\nu = 4.7$, and $r = -3.9$ were employed in the above simulation. For this particular choice of parameters, $\gamma \approx -0.2335$. As predicted by* (3.20), *the curve will initially evolve to increase its length before potentially self-intersecting. Repulsive forces from distal region of the curve kick in to prevent this event, and the curve evolves to increase its length before ultimately filling the numerical box.*

according to (3.28) until the numerical box is full. The motion of the curved domain is eventually arrested by a combination of repulsive forces from the boundary and distal segments of the filament. The reduced asymptotic description of the motion (4.1) does not take into account these nonlocal interactions and therefore only partially describes the full evolution of the one-dimensional filaments studied here.

In Figure 7, nine snapshots of the dynamics of (3.1) are displayed, ranging from the initial profile (top left) to an equilibrium configuration which fills the space (bottom right). For comparison with the reduced asymptotic interface equation (3.20), the parameter values $\gamma = -0.2335$, $\alpha_1 = 0.7892$, $\alpha_2 = 1.0615$ are calculated by quadrature from (3.19). In Figure 8, six snapshots for the corresponding evolution of (3.20) are shown, ranging from an initial ellipse up until self-intersection. The dynamics of the reduced theory capture the lengthening and buckling dynamics of the initial state; however, they do not fully capture the exact quantitative shape of the filament, which appears to be dependent on the nonlocal interactions.
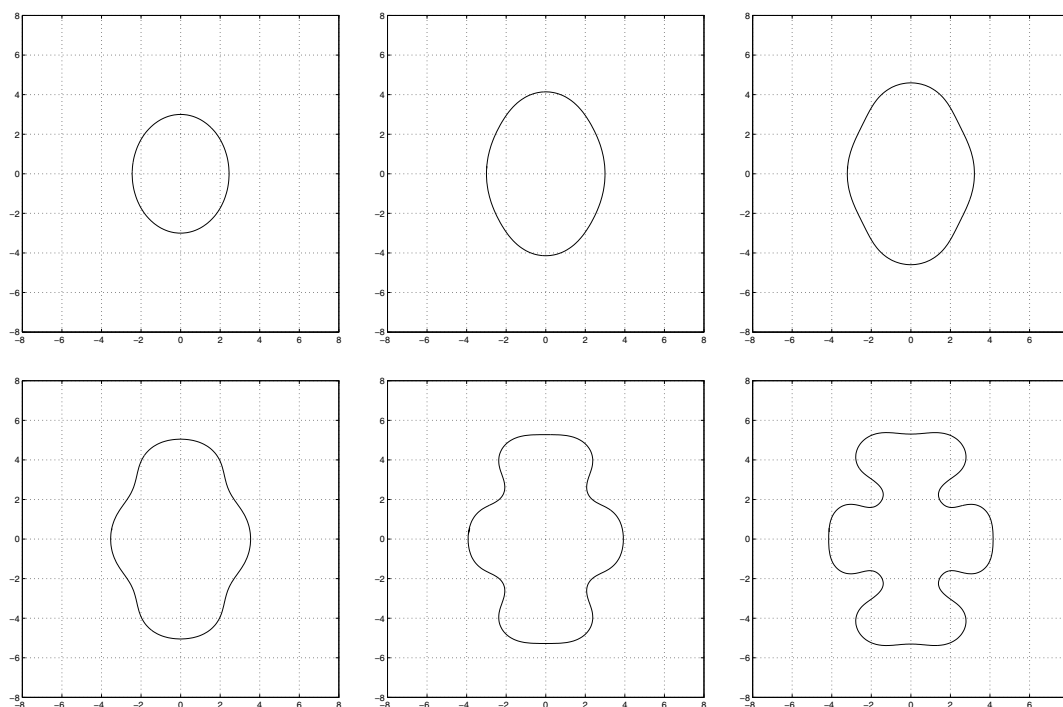
**Figure 8.** *Evolution of* (4.1) *with initial curve* $1.5\,x^2 + y^2 = 9$ *and parameter values* $\epsilon = 0.2$, $\gamma = -0.2335$, $\alpha_1 = 0.7892$, $\alpha_2 = 1.0615$. *The curve buckles and lengthens until it self-intersects.*

There are two main limitations of the asymptotic theory highlighted by the full numerical simulations of Figure 7. First, it is developed under the assumption that $\kappa(s) = \mathcal{O}(1)$ along the length of the filament. As seen in Figure 7, the domain does not maintain this property as the evolution progresses and its labyrinthian pattern becomes more contorted. Second, the asymptotic theory does not account for nonlocal filament interactions which prevent self-intersections. With these two facts in mind, it is only reasonable to expect qualitative agreement of the full system with the reduced asymptotic curve dynamics (4.1) for short time intervals after initialization.

**4.2. Example 2: Curve shortening and convergence to steady radially symmetric solutions.** In this example, the parameter values $\epsilon = 0.2$, $\nu = 4.7$, and $r = -4.2$ are used, which give rise to the one-dimensional profile displayed in Figure 6(b). This profile corresponds to the value $\gamma = 0.1320$ and is of sign opposite that of Example 1. With the parameter $\gamma$ now positive, the analysis of section 3.2 predicts that the curve will evolve to shorten its length. In section 3.3, it was observed that the only equilibrium states of (4.1) corresponding to closed curves were circles. Other closed equilibrium curves were found to be self-intersecting.

In Figure 9, two-dimensional simulations are initialized with nonzero data on a region of width $\epsilon$ centered on the ellipse $1.5\,x^2 + y^2 = 9$, as in Example 1. The curved region contracts and shortens its length until finally converging to a radially symmetric profile centered at the origin. The curves displayed in Figure 10 are simulations of (4.1) for parameter values $\epsilon = 0.2$, $\gamma = 0.1320$, $\alpha_1 = 0.7380$, and $\alpha_2 = 0.5652$, which are calculated from (3.19). The
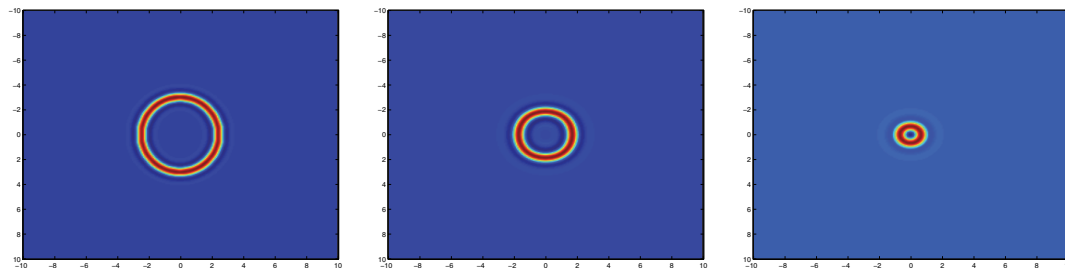
**Figure 9.** *Evolution of* (3.1) *with nonzero initial data provided on the region of distance $\epsilon$ from the ellipse $1.5\,x^2 + y^2 = 9$. The parameter values $\epsilon = 0.2$, $\nu = 4.7$, and $r = -4.2$ were employed in the above simulation. For this particular choice of parameters, $\gamma = 0.1320$. As predicted by* (4.1), *the curve evolves to decrease its length and stabilizes to a radially symmetric solution centered at the origin.*
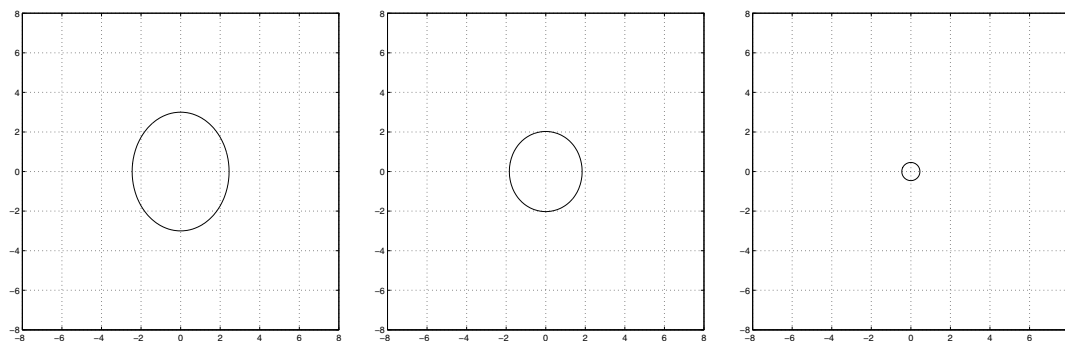


**Figure 10.** *Evolution of* (4.1) *with initial curve $1.5\,x^2 + y^2 = 9$. The parameter values $\epsilon = 0.2$, $\gamma = 0.1320$, $\alpha_1 = 0.7380$, and $\alpha_2 = 0.5652$ were used in the above simulation. As predicted by the equilibrium analysis of section* 3.3, *the initial curve evolves to decrease its length and stabilizes to a circle of radius $R_0 = \epsilon\sqrt{\alpha_2/\gamma} \approx 0.4139$.*

elliptical initial curve equilibrates to a circle with radius $R_0 = \epsilon\sqrt{\alpha_2/\gamma} \approx 0.4139$ in qualitative agreement with the analysis of section 3.3.

To demonstrate the quantitative efficacy of the dynamics predicted by (3.20), radially symmetric solutions of

$$(4.5a) \qquad \epsilon^2 u_t = ru - (1 + \epsilon^2 \Delta_\rho)^2 u + \nu\,v^2 - v^3, \qquad \Delta_\rho \equiv \partial_{\rho\rho} + \rho^{-1}\partial_\rho,$$

on the disc $\{(x,y) \in \mathbb{R}^2 \mid \sqrt{x^2 + y^2} \le R\}$ under boundary conditions

$$(4.5b) \qquad u_\rho = u_{\rho\rho\rho} = 0, \quad \rho = 0; \qquad u = u_\rho = 0, \quad \rho = R,$$

are used for comparison. For radially symmetric solutions, (3.20) predicts that the spike radius $x(t)$ obeys

$$(4.6) \qquad \dot{x} = -\frac{\gamma}{x} + \frac{\alpha_2 \epsilon^2}{x^3}, \qquad x(0) = x_0,$$

and therefore one might expect limiting behavior $x(t) \to x_e \equiv \epsilon\sqrt{\alpha_2/\gamma}$ at $t \to \infty$. However, as discussed in section 4.3, self-interaction effects through the origin can act to arrest spike

(a) Analytical and numerical comparison.



(b) Equilibrium profile.
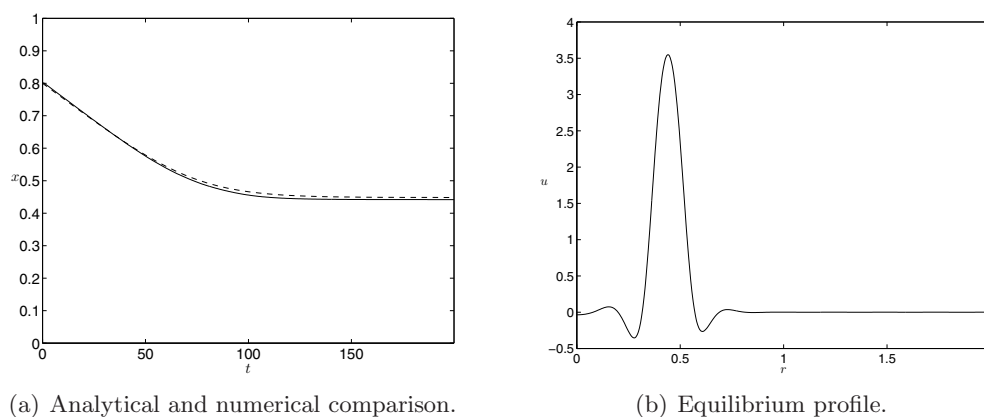
**Figure 11.** *Simulation of* (4.5) *with parameter values* $r = -4.088$, $R = 2$, $\nu = 4.7$, *and* $\epsilon = 0.05$ *initialized with a single spike centered at* $\rho = 0.8$. *(a) A comparison of the numerical spike location (solid) with the analytical prediction (dashed) of* (4.6). *(b) The solution profile at equilibrium.*

motion. Consequently, there are two possible scenarios. First, if $x_e$ is large enough, then the spike is pinned by the dynamics of (4.6) and not by self-interaction forces at the origin. Second, $x_e$ is smaller than the length scale on which self-interaction forces act, and the spike is pinned at a radius before that predicted by (4.6).

To control the size of $x_e$ for a fixed $\epsilon$, recall that for fixed $\nu = 4.7$, $r = -3.9$ corresponds to $\gamma < 0$, while $r = -4.2$ yields a $\gamma > 0$. Assuming a continuous dependence of $\gamma$ on $r$, it follows that there exists a critical value $r_c$ such that $\gamma(r_c) = 0$ (cf. Figure 2(b)). For a fixed $\epsilon$, the size of $x_e$ can therefore be made arbitrarily large by tuning the parameter $r$ such that $\gamma(r)$ is arbitrarily small but positive. This motivates the following two experiments, both with common parameters, $R = 2$, $\epsilon = 0.05$, and $\nu = 4.7$.

*Experiment* 1. Using $r = -4.088$ results in $\gamma \approx 0.0054$, $a_2 \approx 0.4367$, and $x_e \approx 0.4483$. As shown in Figure 11, the spike is equilibrated by the dynamics of (4.6) before getting close enough to the origin to experience self-repulsion. The final profile at equilibrium is shown in Figure 11(b). Note that since $\gamma$ is very small, equilibration occurs on a long time scale.

*Experiment* 2. Using $r = -4.2$ results in $\gamma \approx 0.1320$, $a_2 \approx 0.5652$, and $x_e \approx 0.1035$. From the simulation of Figure 12(a), we see that spike motion is arrested before the equilibria predicted by (4.6). Indeed, the equilibrium profile displayed in Figure 12(b) has fully interacted with the origin.

**4.3. Repulsion of nearby curves.** The analysis of section 3 assumes no interaction between the tail of a particular localized structure and that of separate structures centered on distant sections of the curve centerline. Given appropriate initial conditions, and the fact that the base profile (3.5) decays exponentially quickly in its far field, this assumption seems reasonable. As the coherent structure evolves according to (3.20), self-intersection of the curve becomes a possibility. In numerical simulations it is observed that at some characteristic length scale, forces emerge to stabilize the separation distance, regardless of the wide range of possible incidence angles.

(a) Analytical and numerical comparison.



(b) Equilibrium profile.
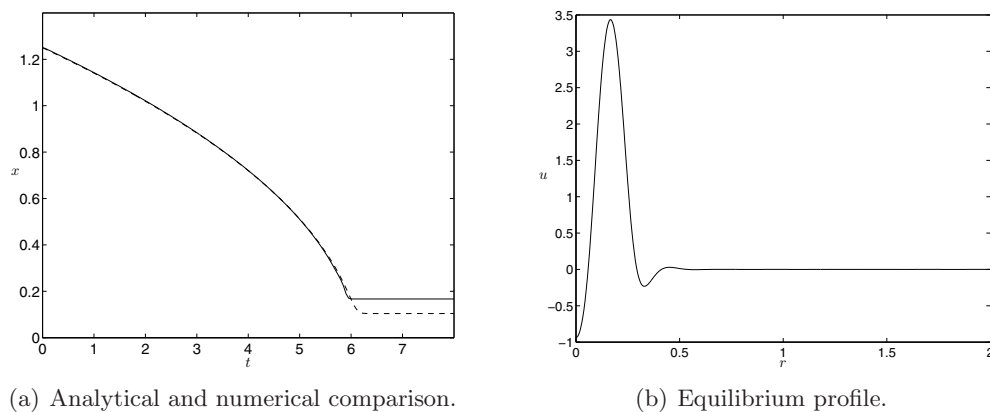
**Figure 12.** *Simulation of* (4.5) *with parameter values* $r = -4.2$, $R = 2$, $\nu = 4.7$, *and* $\epsilon = 0.05$ *initialized with a single spike centered at* $\rho = 1.25$. (a) *A comparison of the numerical spike location (solid) with the analytical prediction (dashed) of* (4.6). (b) *The solution profile at equilibrium.*

The procedure outlined by Elphick, Meron, and Spiegel [10] predicts the dynamics of superpositions of multiple exponentially decaying stable localized structures and provides some explanation for the observed stabilization of the self-intersecting curve. We reproduce this argument for our problem to illustrate the qualitative effects that nearby structures have on the motion of a localized solution.

An approximate superposition of $n$ well-separated one-dimensional profiles $v_0(x)$ of (3.5) on $\mathbb{R}$ can be written

$$(4.7) \qquad v(x, \tau) = \sum_{i=1}^{n} v_i + \delta R(x, \tau), \quad v_i \equiv v_0(x - x_i(\tau)),$$

where $\tau = \delta t$ is the slow time scale for motion and $x_i(\tau)$ is the peak of each isolated profile. The perturbation parameter here is $\delta = \exp[-aL]$, where $L$ is an assumed large characteristic length scale between isolated peaks. The dynamic equation can be decomposed into linear and nonlinear parts,

$$(4.8) \qquad u_t = \mathcal{L}u + N(u), \quad \mathcal{L}u \equiv ru - \left(1 + \frac{\partial^2}{\partial x^2}\right)^2 u.$$

Inserting this ansatz into the dynamic equation, the correction term $R$ to leading order satisfies

$$(4.9) \qquad \left(\mathcal{L} + N'\left(\sum_{i=1}^{n} v_i\right)\right) R \sim -\sum_{i=1}^{n} \left(\frac{\partial v_i}{\partial x}\right) \dot{x}_i + N\left(\sum_{i=1}^{n} v_i\right) - \sum_{i=1}^{n} N(v_i).$$

The linear operator on the left-hand side of (4.9) is, to the same level of approximation, just the sum of linearizations about each steady state solution $v_i$. One can therefore use approximate eigenfunctions $\partial v_i / \partial x$ in a Fredholm-type argument (see, e.g., [14]) to arrive at
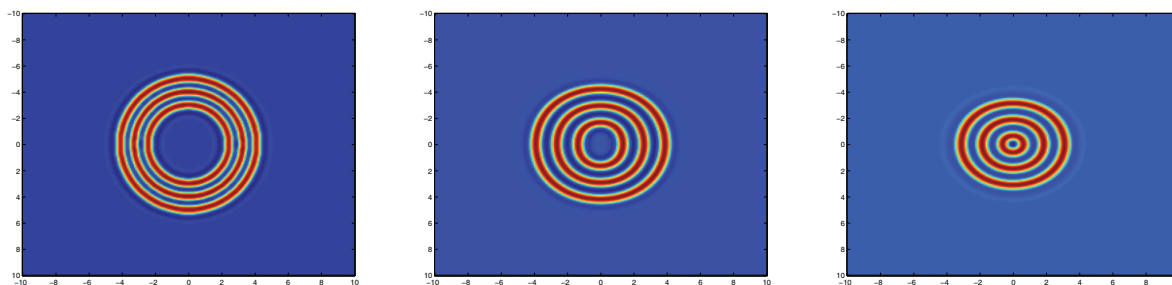
**Figure 13.** *Evolution of* (3.1) *with nonzero initial data provided on the regions of distance $\epsilon$ from the ellipses $1.5\,x^2 + y^2 = 9$, $1.5\,x^2 + y^2 = 16$, and $1.5\,x^2 + y^2 = 25$. The parameter values $\epsilon = 0.2$, $\nu = 4.7$, and $r = -4.2$ were employed in the above simulation. For this particular choice of parameters, $\gamma \approx 0.1320$. The curve evolves to decrease its length and stabilizes to a multipeak radially symmetric solution centered at the origin.*

an expression for the leading order dynamics:

$$(4.10) \qquad \dot{x}_i = \sum_{\substack{j=1 \\ j \neq i}}^{n} \frac{\int_{-\infty}^{\infty} N'(v_j) v_i (\frac{\partial v_j}{\partial x}) dx}{\int_{-\infty}^{\infty} (\frac{\partial v_j}{\partial x})^2 dx}, \qquad i = 1, \dots, n.$$

The qualitative nature of interaction is captured by the integral in the numerator of (4.10), which involves the oscillating tail of $v_i$. As the relative distance between peaks $|x_i - x_j|$ varies, the character of interaction alternates between attractive and repulsive in a relatively periodic fashion. In a multidimensional setting, once two curves are reasonably close, the magnitude of interaction can become as significant as the other geometric effects, as we will numerically illustrate.

Figure 13 displays simulations of (3.1) initialized with regions of width $\epsilon$ centered on the ellipses $1.5\,x^2 + y^2 = 9$, $1.5\,x^2 + y^2 = 16$, and $1.5\,x^2 + y^2 = 25$. The inhomogeneities of the initial data are smoothed out by the dynamics, which are length shortening as described by the theory of section 3.2. Once short term interactions come into play and arrest curve motion, the limiting behavior is to a radially symmetric profile consisting of three rings.
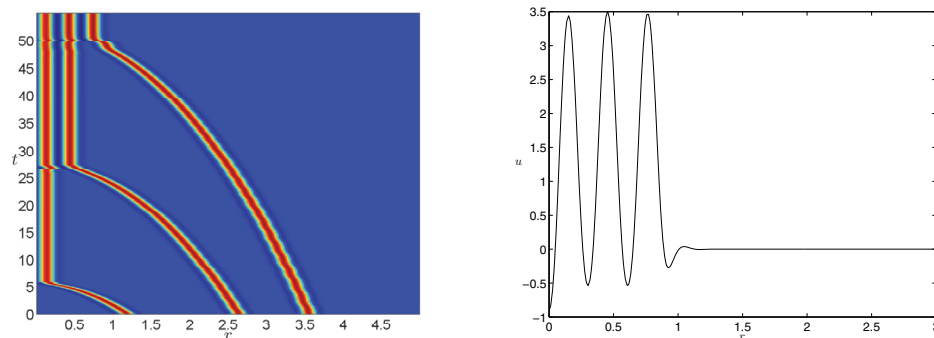
In Figure 14, numerically obtained radially symmetric solutions of (4.5) with parameters $R = 5$, $r = -4.2$, $\nu = 4.7$, and $\epsilon = 0.05$ are displayed. Simulations are initialized with three spikes centered at $(x_1(0), x_2(0), x_3(0)) = (1.2, 2.64, 3.55)$. The parameter values chosen (the same as in Example 2) give rise to $\gamma \approx 0.1320$, $\alpha_1 \approx 0.7380$, $\alpha_2 \approx 0.5646$.

**5. Conclusion.** There has been significant recent interest regarding the existence, multiplicity, and stability of one-dimensional localized states $u_0(x)$ of the Swift–Hohenberg equation,

$$(5.1) \qquad r\,u_0 - \left(1 + \frac{d^2}{dx^2}\right)^2 u_0 + \nu\,u_0^2 - u_0^3 = 0, \qquad u_0 : \mathbb{R} \to \mathbb{R}; \qquad u_0 \to 0, \quad |x| \to \infty.$$

Surprisingly, a large family of one-dimensional solutions to (5.1) exist in a parameter interval surrounding the Maxwell point. This phenomenon is known as *snakes and ladders* due to

(a) Space time diagram of radially symmetric solutions.

(b) Three-spike equilibrium profile.

**Figure 14.** *Numerical simulations of* (4.5) *initialized with three spikes and parameter values* $r = -4.2$, $\nu = 4.7$, *and* $\epsilon = 0.05$. *Panel* (a) *displays the space time diagram of the solution and shows the evolution of the three spikes and their eventual uniform equilibration spacing. Panel* (b) *shows the equilibrium configuration consisting of three maxima.*

the intertwining nature of the stable and unstable branches (snakes) coupled with the interconnecting asymmetric solution branches (ladders). The main aim of this paper has been to study the stability and dynamics of stable one-dimensional states in a two-dimensional setting and to consequently shed light on possible equilibrium configurations of the problem

$$(5.2) \qquad r\,u - (1 + \Delta)^2\,u + \nu\,u^2 - u^3 = 0, \qquad u : \mathbb{R}^2 \to \mathbb{R}; \qquad u \to 0, \quad |x| \to \infty.$$

In section 2, a sufficiency condition for a stable solution $u_0(x)$ of (5.1) to be a stable stripe solution of (5.2) was established. In terms of $\lambda_1$, the largest nonzero eigenvalue of the linearization of (5.1) about $u_0(x)$, we show that whenever $\lambda_1 < -1$, $u_0(x)$ is a stable stripe solution of (5.2). In other words, if $u_0(x)$ is a stable *enough* solution of (5.1), then $u(x, y) = u_0(x)$ is a stable solution of (5.2).

When this situation arises, filaments whose cross sections are formed by $u_0(x)$ can be constructed and their resulting dynamics analyzed. In section 3, it was established by means of a fitted orthogonal system that the normal velocity for the centerline of a filament of width $\epsilon \ll 1$ satisfies

$$(5.3) \qquad \rho_t = -2\kappa \left( \frac{\langle u_0'', u_0'' \rangle}{\langle u_0', u_0' \rangle} - 1 \right) + \epsilon^2 \left( \alpha_1 \kappa_{ss} + \alpha_2 \kappa^3 \right) + \cdots$$

in the limit as $\epsilon \to 0$. In expression (5.3), $\kappa(s) = \mathcal{O}(1)$ is the curvature of the filament, while the constants $\alpha_1$, $\alpha_2$ are known quantities determined in (3.19). The coefficient of the curvature term in (5.3) has appeared previously as $\lambda_2$ in (2.8) and $\gamma$ in (3.21), and its sign is found to predict the qualitative dynamics of the filament. The higher order terms provide elastic regularization of the geometric motion. An analysis of (5.3) reveals the existence of meandering and circular steady states. However, noncircular closed equilibrium curves are found to be self-intersecting.

When the dynamics of (5.3) do not arrest curve-motion, self-interaction of the evolving structure is prevented by repulsive forces generated by the interaction of exponentially decaying tails from distal filament segments. When $\gamma < 0$, the filaments evolve to length shorten and equilibrate on radially symmetric solutions. Interestingly, when simulations are initialized with multiple filaments, the structure evolves to radially symmetric multipeak equilibria. For $\gamma > 0$, curve-lengthening occurs before motion is arrested by interaction with the boundary and results in a space-filling equilibrium.

While the asymptotic description of (5.3) incorporates many of the mechanisms of filament evolution observed in the full system, the absence of nonlocal interactions is a conspicuous limiting feature. It would therefore be very interesting to incorporate such effects in a systematic way, to arrive at a hybrid geometric and nonlocal description of domain evolution.

## REFERENCES

[1] J. Arroyo, O. Garay, and J. Mencia, *When is a periodic function the curvature of a closed plane curve?*, Amer. Math. Monthly, 115 (2008), pp. 405–414.

[2] D. Avitabile, D. J. B. Lloyd, J. Burke, E. Knobloch, and B. Sandstede, *To snake or not to snake in the planar Swift–Hohenberg equation*, SIAM J. Appl. Dyn. Syst., 9 (2010), pp. 704–733.

[3] M. Beck, J. Knobloch, D. J. B. Lloyd, B. Sandstede, and T. Wagenknecht, *Snakes, ladders, and isolas of localized patterns*, SIAM J. Math. Anal., 41 (2009), pp. 936–972.

[4] J. Burke and E. Knobloch, *Localized states in the generalized Swift-Hohenberg equation*, Phys. Rev. E, 73 (2006), 056211.

[5] A. Di Carlo, M. E. Gurtin, and P. Podio-Guidugli, *A regularized equation for anisotropic motion-by-curvature*, SIAM J. Appl. Math., 52 (1992), pp. 1111–1119.

[6] S. J. Chapman and G. Kozyreff, *Exponential asymptotics of localised patterns and snaking bifurcation diagrams*, Phys. D, 238 (2009), pp. 319–354.

[7] D. L. Chopp and J. A. Sethian, *Motion by intrinsic Laplacian of curvature*, Interfaces Free Bound., 1 (1999), pp. 1–18.

[8] M. C. Cross and P. C. Hohenberg, *Pattern formation outside of equilibrium*, Rev. Modern Phys., 65 (1993), pp. 851–1112.

[9] J. H. P. Dawes, *The emergence of a coherent structure for coherent structures: Localized states in nonlinear systems*, Roy. Soc. London Phil. Trans. Ser. A, 368 (2010), pp. 3519–3534.

[10] C. Elphick, E. Meron, and E. A. Spiegel, *Patterns of propagating pulses*, SIAM J. Appl. Math., 50 (1990), pp. 490–503.

[11] L. C. Evans and J. Spruck, *Motion of level sets by mean curvature*, J. Differential Geom., 33 (1991), pp. 635–681.

[12] P. C. Fife, *Dynamics of Internal Layers and Diffuse Interfaces*, CBMS-NSF Regional Conf. Ser. in Appl. Math. 53, SIAM, Philadelphia, 1988.

[13] N. Gavish, G. Hayrapetyan, K. Promislow, and L. Yang, *Curvature driven flow of bi-layer interfaces*, Phys. D, 240 (2011), pp. 675–693.

[14] K. B. Glasner, *Spatially localized structures in diblock copolymer mixtures*, SIAM J. Appl. Math., 70 (2010), pp. 2045–2074.

[15] R. E. Goldstein, D. J. Muraki, and D. M. Petrich, *Interface proliferation and the growth of labyrinths in a reaction-diffusion system*, Phys. Rev. E, 53 (1996), pp. 3933–3957.

[16] E. Knobloch, *Spatially localized structures in dissipative systems: Open problems*, Nonlinearity, 21 (2008), pp. 45 ff.

[17] J. Knobloch and T. Wagenknecht, *Homoclinic snaking near a heteroclinic cycle in reversible systems*, Phys. D, 206 (2005), pp. 82–93.

[18] T. Kolokolnikov, W. Sun, M. Ward, and J. Wei, *The stability of a stripe for the Gierer–Meinhardt model and the effect of saturation*, SIAM J. Appl. Dyn. Syst., 5 (2006), pp. 313–363.

[19] T. Kolokolnikov, M. Ward, and J. Wei, *Self-replication of mesa patterns in reaction-diffusion systems*, Phys. D, 236 (2007), pp. 104–122.

[20] B. Li, J. Lowengrub, A. Ratz, and A. Voigt, *Geometric evolution laws for thin crystalline films: Modeling and numerics*, Comm. Comput. Phys., 6 (2009), pp. 433–482.

[21] D. Lloyd and B. Sandstede, *Localized radial solutions of the Swift-Hohenberg equation*, Nonlinearity, 22 (2009), pp. 485–524.

[22] D. J. B. Lloyd, B. Sandstede, D. Avitabile, and A. R. Champneys, *Localized hexagon patterns of the planar Swift–Hohenberg equation*, SIAM J. Appl. Dyn. Syst., 7 (2008), pp. 1049–1100.

[23] S. McCalla and B. Sandstede, *Snaking of radial solutions of the multi-dimensional Swift-Hohenberg equation: A numerical study*, Phys. D, 239 (2010), pp. 1581–1592.

[24] C. B. Muratov, *Theory of domain patterns in systems with long-range interactions of Coulomb type*, Phys. Rev. E, 66 (2002), 066108.

[25] C. B. Muratov and V. V. Osipov, *Scenarios of domain pattern formation in a reaction-diffusion system*, Phys. Rev. E, 54 (1996), pp. 4860–4879.

[26] Y. Nishiura and D. Ueyama, *A skeleton structure of self-replicating dynamics*, Phys. D, 130 (1999), pp. 73–104.

[27] Y. Pomeau, *Front motion, metastability and subcritical bifurcations in hydrodynamics*, Phys. D, 23 (1986), pp. 3–11.

[28] W. N. Reynolds, J. E. Pearson, and S. Ponce-Dawson, *Dynamics of self-replicating patterns in reaction diffusion systems*, Phys. Rev. Lett., 72 (1994), pp. 2797–2800.

[29] P. Smereka, *Semi-implicit level set methods for curvature and surface diffusion motion*, J. Sci. Comput., 19 (2003), pp. 439–456.

[30] P. D. Woods and A. R. Champneys, *Heteroclinic tangles and homoclinic snaking in the unfolding of a degenerate reversible Hamiltonian-Hopf bifurcation*, Phys. D, 129 (1999), pp. 147–170.